https://doi.org/10.5194/tc-2020-211
Preprint. Discussion started: 25 August 2020

The Cryosphere Discussions

Seasonal changes in sea ice kinematics and deformation in the Pacific Sector of the Arctic Ocean in 2018/19

Ruibo Lei[1], Mario Hoppmann[2], Bin Cheng[3], Guangyu Zuo[1,4], Dawei Gui[1,5], Qiongqiong Cai[6], H. Jakob Belter[2], Wangxiao Yang[4]

[1] Key Laboratory for Polar Science of the MNR, Polar Research Institute of China, Shanghai, China.

[2]Alfred-Wegener-Institut Helmholtz-Zentrum für Polar- und Meeresforschung, Bremerhaven, Germany.

[3] Finnish Meteorological Institute, Helsinki, Finland.

[4] College of Electrical and Power Engineering, Taiyuan University of Technology, Taiyuan, China.

[5] Chinese Antarctic Center of Surveying and Mapping, Wuhan University, Wuhan, China.

[6] National Marine Environmental Forecasting Center of the MNR, Beijing, China.

Correspondence to: Ruibo Lei (leiruibo@pric.org.cn)

Abstract. Arctic sea ice kinematics and deformation play significant roles in heat and momentum exchange between atmosphere and ocean. However, mechanisms regulating their changes at seasonal scales remain poorly understood. Using position data of 32 buoys in the Pacific sector of the Arctic Ocean (PAO), we characterized spatiotemporal variations in ice kinematics and deformation for autumn–winter 2018/19. In autumn, sea ice drift response to wind forcing and inertia were stronger in the southern and western than in the northern and eastern parts of the PAO. These spatial heterogeneities decreased gradually from autumn to winter, in line with the seasonal evolution of ice concentration and thickness. Areal localization index decreased by about 50 % from autumn to winter, suggesting the enhanced localization of intense ice deformation as the increased ice mechanical strength. In winter 2018/19, a highly positive Arctic Dipole and a weakened high pressure system over the Beaufort Sea led to a distinct change in ice drift direction and an temporary increase in ice deformation. During the freezing season, ice deformation rate in the northern part of the PAO was about 2.5 times that in the western part due to the higher spatial heterogeneity of oceanic and atmospheric forcing in the north. North–south and east–west gradients in sea ice kinematics and deformation of the PAO observed in autumn 2018 are likely to become more pronounced in the future as sea ice losses at higher rates in the western and southern than in the northern and western parts.

https://doi.org/10.5194/tc-2020-211
Preprint. Discussion started: 25 August 2020

1 Introduction

The Pacific sector of Arctic Ocean (PAO) includes the Beaufort, Chukchi, and East Siberian Seas, as well as the Canadian and Makarov Basins. Among all the sectors of the Arctic Ocean, decreases in both summer sea ice (Comiso et al., 2017) and multi-year sea ice (MYI) (Serreze and Meier, 2018) are the largest in the PAO in recent decades, and are most likely linked to the Arctic Amplification (Serreze and Barry, 2011), enhanced ice–albedo feedback (Steele and Dickinson, 2016), increased Pacific water inflow (Woodgate et al., 2012), and enhanced Arctic Dipole (Lei et al., 2016). In the PAO, MYI is mainly distributed north of the Canadian Arctic Archipelago (Lindell and Long, 2016), suggesting a strong east–west gradient in sea ice thickness and strength. In summer, the marginal ice zone (MIZ), defined as the area where sea ice concentration is less than 80 %, can reach as far north as 80° N (Strong and Rigor, 2013), thus the south–north gradient in ice conditions in the PAO is expected to be greater than that in other sectors of the Arctic Ocean.

Sea ice deformation results from divergence, convergence, and shear of ice floes (Hutchings and Hibler, 2008). Loss of MYI and decreased ice thickness weakens the Arctic ice cover, increases floe mobility (Spreen et al., 2011), and promotes ice deformation (Kwok, 2006), which further enhances redistribution of ice thickness by producing leads and ridges (Itkin et al., 2018). Leads between ice floes increase heat loss from the ice-covered ocean to the atmosphere. This process is particularly important in winter because of the large temperature gradient (Alam and Curry, 1998), and contributes considerably to the Arctic Amplification (Lüpkes et al., 2008). Cracks or leads in the pack ice serve as windows that expose the ocean to sunlight, promoting under-ice haptophyte algae blooms (Assmy et al., 2017). Especially under converging conditions, ice blocks are packed randomly during the formation of sea ice pressure ridges, creating water-filled voids that act as thermal buffers for subsequent ice growth (Salganik et al., 2020). The high porosity of pressure ridges results in an abundance of nutrients for ice algae communities. As a result, pressure ridges can become biological hotspots (Fernández-Méndez et al., 2018). Thus, characterizations of sea ice deformation are relevant for a better understanding of ice dynamics and their roles in current changes in Arctic climate system, and also of ice-associated ecosystems.

https://doi.org/10.5194/tc-2020-211
Preprint. Discussion started: 25 August 2020

In the PAO, the generally anticyclonic Beaufort Gyre (BG) generates sea ice motion that is clockwise on average. The boundary and strength of the BG are mainly regulated by the Beaufort High (BH) (Proshutinsky et al., 2009; Lei et al., 2019). Anomalously low BH can result in a reversal of wind and ice motion in the PAO that is normally anticyclonic (Moore et al., 2018). Under a positive Arctic Dipole Anomaly (DA), more sea ice from the PAO is transported to the Atlantic sector of the Arctic Ocean, i.e., promoting ice advection from the BG system to the Transpolar Drift Stream (TDS) (Wang et al., 2009). In summer, such a regime would stimulate the ice–albedo feedback and accelerate sea ice retreat (Lei et al., 2016). Response of sea ice advection in this region to interannual variation of atmospheric circulation patterns has been studied extensively (e.g., Vihma et al., 2012), but investigations on a seasonal scale are relatively scarce.

From a dynamical perspective, sea ice consolidation has been quantified using the strength of the inertial signal of sea ice motion (Gimbert et al., 2012), Ice–Wind Speed Ratio (IWSR) (Haller et al., 2014), localization, intermittence and space–time coupling of sea ice deformation (Marsan et al., 2004), as well as response of ice deformation to wind forcing (Haller et al., 2014). The localization and intermittence of ice deformation indicate the degree of constraint for the spatial range and temporal duration of sea ice deformation (Rampal et al., 2008). Space-time coupling demonstrates the temporal or spatial dependence for the spatial or temporal scaling laws of ice deformation, which can indicate the brittle behaviour of sea ice deformation (Rampal et al., 2008; Marsan and Weiss, 2010). The inertial oscillations of ice motion (Gimbert et al., 2012) and the IWSR (Spreen et al., 2011) have been demonstrated to increase as a result of reduced sea ice thickness and concentration. However, effects of sea ice consolidation on its kinematics and deformation on synoptic and seasonal scales remain unclear. Furthermore, because the number of buoys deployed in any given season and sector of the Arctic Ocean has been limited, it has so far been difficult to accurately distinguish spatial variability and temporal change in sea ice kinematics and deformation from existing buoy data. During spring 2003, the deformation of a single lead in the Beaufort Sea was investigated using four Global Positioning System (GPS) receivers, and the data has been used to estimate the opening rate and shear of the lead (Hutchings and Hibler, 2008). Based on the dispersion characteristics of ice motion estimated using the data obtained from 22 buoys deployed on the ice in the south of Beaufort Sea, Lukovich et al. (2011) found that the scaling law of absolute zonal dispersion is about twice that at the meridional direction, which implicates the gradient of sea ice motion in the zonal direction is much larger than that in the meridional direction. Lei et al. (2020a and 2020b) used data measured by two buoy arrays deployed in the north of PAO to describe the influence of cyclonic activities and summer ice regime on seasonal evolution in sea ice deformation, and found that the summer ice regime has a continuous effect on the sea ice deformation in autumn and winter. However, the full picture of spatial and seasonal variations of sea ice kinematics and deformation for the whole PAO region has not been described using the buoy data in the previous literatures. High resolution satellite images (e.g., Kwok, 2006) and sea ice numerical models (e.g., Hutter et al., 2018) can be used to identify spatial and temporal variations of ice deformation at the basin scale. However, their abilities to correctly describe ice deformation, which usually occurs in small scales and over short periods (Hutchings and Hibler, 2008), still need ground-truthing data for example collected by buoy arrays to assess.

During August and September 2018, 27 drifting buoys were deployed on sea ice in the PAO by the Chinese National Arctic Research Expedition (CHINARE) and the T-ICE expedition. We combined the data measured by these buoys and other available buoy data from the International Arctic Buoy Programme (IABP) to identify the spatial variability of sea ice kinematic and deformation parameters in the PAO from melting to freezing season, and locate the atmospheric forcing parameters responsible to the ice dynamic changes.

2 Data and Methods

2.1 Deployment of drifting buoys

Four types of buoys were used in this study (Fig. 1). They are the Snow and Ice Mass Balance Array (SIMBA) buoy manufactured by Scottish Association for Marine Science Research Services Ltd, Oban, Scotland, the Snow Buoy (SB) designed by the Alfred-Wegener-Institute and manufactured by MetOcean Telematics, Halifax, Canada, the ice Surface Velocity Program drifting buoy (iSVP) also manufactured by MetOcean Telematics, and the ice drifter manufactured by the Taiyuan University of Technology (TUT), China. Although the buoys were equipped with different types of GPS receivers, they all have a positioning accuracy of better than 5 m.

During the CHINARE, 9 SIMBA buoys and 11 TUT buoys were deployed in a narrow zonal section between 156° W and 171° W and a wide meridional range between 79.2° N and 84.9° N in August 2018 (Figs. 1 and 2). This deployment scheme was designed to facilitate the analysis of ice kinematic characteristics from the loose MIZ to the consolidated Pack Ice Zone (PIZ). From these 20 buoys, 15 were deployed in the northern part of the PAO as a cluster within close distance of each other (black circles in Fig. 2) to allow estimation of ice deformation rates. In addition, data from five SIMBAs and two SBs deployed by the T-ICE expedition in the Makarov Basin during September 2018 (Figs. 1 and 2) were also used to estimate ice deformation rates. Because the ice thickness at the deployment sites on both expeditions was comparably large (1.22 to 2.49 m), the buoys were able to survive into winter and beyond. Position data from one iSVP buoy deployed during the previous CHINARE in 2016 (Lei et al., 2020a) and four other IABP buoys were also included in this study. The IABP buoys were deployed by the British Antarctic Survey and Environment Canada in the east of the PAO during late August or late September 2018. Here we use the position data from these 32 buoys to analyze spatial variations in ice kinematics (Fig. 2) between August 2018 and February 2019. We chose this study period because it represents the transition from late summer to winter, a period during which the mechanical properties of sea ice are expected to change considerably (e.g., Herman and Glowacki, 2012; Hutter et al., 2018). Also, some buoys have ceased operation by March 2019. Two-thirds of the buoys (22) continued to send data until or beyond the end of the study period. To identify the spatial variability of atmospheric forcing and sea ice conditions, the study region is defined as 76° N–87° N and 155° E–110° W.

2.2 Analysis of sea ice kinematic characteristics

All buoys have a sampling interval of either 0.5 or 1 h. Prior to the calculation of ice drift velocity, position data measured by the buoys were interpolated to a regular interval (τ) of 1 h. To quantify meridional (zonal) variabilities of ice kinematic properties, we used data from buoys that were within one standard deviation of the average longitude (latitude), which helps to minimize influence of zonal (meridional) difference on meridional (zonal) variabilities. Meridional variabilities can be used to detect the transition from the MIZ to the PIZ, while zonal variabilities can indicate the change between the region north of the Canadian Arctic Archipelago, where MYI coverage is usually large (Lindell and Long, 2016) and the Makarov Basin, which is mainly covered by seasonal sea ice (Serreze and Meier, 2018).

Two parameters were used to characterize sea ice kinematic properties. First, IWSR was used to investigate the response of sea ice motion to wind forcing. Impacts of resampling wind speed and ice position data at various intervals between 1 and 48 h, meridional and zonal spatial variabilities,

https://doi.org/10.5194/tc-2020-211
Preprint. Discussion started: 25 August 2020

intensity of wind forcing, near-surface air temperature, and ice concentration on IWSR were assessed. The data used to characterize atmospheric forcing, including Sea Level air Pressure (SLP), near-surface air temperature at 2 m (T_{2m}) and wind velocity at 10 m (W_{10m}) were obtained from the ECMWF ERA-Interim reanalysis (Dee et al., 2011). Sea ice concentration for the study period was obtained from the Advanced Microwave Scanning Radiometer 2 (AMSR2) (Spreen et al., 2008). To identify the state of atmospheric forcing and ice conditions relative to the climatology, we also calculated anomalies of SLP, T_{2m}, W_{10m}, ice concentration, and ice drift speed relative to the 1979–2018 averages. To estimate ice concentration anomalies, we used ice concentration data from the Nimbus-7 Scanning Multichannel Microwave Radiometer (SMMR) and its successors (SSM/I and SSMIS) (Fetterer et al., 2017) because they cover a longer period than AMSR2 data. We used the daily product of sea ice motion (Fowler et al., 2013) provided by the National Snow and Ice Data Center (NSIDC) to estimate ice drift speed anomalies. Because of the delayed release of NSIDC data, ice drift speed anomalies were only estimated for August–December 2018.

Second, the inertial motion index (IMI) was used to quantify the inertial component of ice motion. Its magnitude can indicate the free-drift property of ice motion (Gimbert et al., 2012). To obtain the IMI, we applied a Fast Fourier Transformation to normalized hourly ice velocities. Normalized ice velocities were calculated by scaling velocity values to monthly average velocity values, allowing seasonal change to be assessed independently of differences in absolute magnitudes of ice velocities between buoys. The frequency of the inertial oscillation varies with latitude as follows:

$$f_0 = 2\Omega \sin\theta \qquad (1)$$

where f_0 is inertial frequency, Ω is earth rotation rate, and θ is latitude. Inertial frequency ranges from 2.01 to 1.94 cycles day^{-1} between 90° N and 75° N. Rotary spectra calculated from sea ice velocity using complex Fourier analysis were used to identify signals of inertial and tidal origin, both of which have a frequency of about 2 cycles day^{-1} in the Arctic Ocean (Gimbert et al., 2012). According to Gimbert et al. (2012), the complex Fourier transformation $\widehat{U}(\omega)$ is defined as:

$$\widehat{U}(\omega) = \frac{1}{N}\sum_{t=t_0}^{t_{end}-\Delta t} e^{-i\omega t}\left(u_x + iu_y\right), \qquad (2)$$

where N and Δt are the number and temporal interval of velocity samples, t_0 and t_{end} are the start and end times of the temporal window, u_x and u_y are zonal and meridional ice speeds at $t+0.5\Delta t$ on an orthogonal geographical grid, and ω is angular frequency. The IMI was defined as the amplitude at the inertial frequency after the complex Fourier transformation.

2.3 Analysis of sea ice deformation characteristics

Ice positions were used to estimate differential kinematic properties (DKPs) of the sea ice deformation field. The DKPs include divergence rate (*div*), shear rate (*shr*), and total deformation rate (*D*) of sea ice within the area enclosed by any three buoys. Following Hutchings and Hibler (2008), DKPs were calculated as follows:

$$div = \frac{\partial u}{\partial x} + \frac{\partial v}{\partial y} \ , \tag{3}$$

$$shr = \sqrt{\left(\frac{\partial u}{\partial x} - \frac{\partial v}{\partial y}\right)^2 + \left(\frac{\partial u}{\partial y} + \frac{\partial v}{\partial x}\right)^2} \ , \tag{4}$$

and $D = \sqrt{div^2 + shr^2}$, (5)

where $\frac{\partial u}{\partial x}$, $\frac{\partial v}{\partial y}$, $\frac{\partial u}{\partial y}$, and $\frac{\partial v}{\partial x}$ are the strain components on an orthogonal geographical grid. Sea ice strain rate was estimated only for buoy triangles with internal angles in excess of 15° and for ice speeds > 0.02 m s^{-1} to ensure accuracy (Hutchings et al., 2012). Total deformation D was used to characterize the spatial and temporal scaling laws as follows:

$$D \propto L^{-\beta}, \tag{6}$$

and $D \propto \tau^{-\alpha}$, (7)

where L is length scale, τ is sampling interval, and β and α are spatial and temporal scaling exponents, which indicate decay rates of the sea ice deformation in spatial or temporal domains. To estimate spatial exponent β, length scale was divided into three bins of 5–10, 10–20, and 20–40 km for the CHINARE buoy cluster because only few samples were outside these bins. To estimate temporal exponent α, position data were resampled at intervals of 1, 2, 4, 8, 12, 24, and 48 h. Because the T-ICE buoy cluster was mostly (> 70 %) in the bin of 40–80 km, data from this cluster were unsuitable for the characterization of scale effect. Space–time coupling index, c, denoting temporal (spatial) dependence of the spatial (temporal) scaling exponent, can be expressed as:

$$\beta(\tau) = \beta_0 - c\ln(\tau), \tag{8}$$

https://doi.org/10.5194/tc-2020-211
Preprint. Discussion started: 25 August 2020

where β_0 is a constant. The areal localization index, $\delta_{15\%}$, was used to quantify localization of the strongest sea ice deformation, which is defined as the fractional area accommodating the largest 15 % of the ice deformation (Stern and Lindsay, 2009). The $\delta_{15\%}$ was calculated for the length bin of 10–20 km for the CHINARE buoy cluster because this bin contained most of the data. To identify the influence of temporal scale on localization of ice deformation, data were resampled at intervals of 1, 2, 4, 8, 12, 24, and 48 h.

2.4 Atmospheric circulation pattern

To identify the influence of atmospheric circulation patterns on sea ice kinematics and deformation, we calculated the seasonal Central Arctic Index (CAI) and DA index to relate the potential of the northward advection of sea ice from the study region to the Atlantic sector of the Arctic Ocean, and the seasonal AO and BH indices to relate the strength of BG. Monthly SLP data north of 70° N obtained from the NCEP/NCAR reanalysis I were used to calculate the empirical orthogonal function modes, with the AO and DA as the first and second modes (Wang et al., 2009). The CAI was defined as the difference in SLP between 90° W and 90° E at 84° N (Vihma et al., 2012). The BH index was calculated as the average SLP anomaly over the domain of 75° N–85° N, 170° E–150° W (Moore et al., 2018) relative to 1979–2018 climatology.

3 Results

3.1 Spatiotemporal changes in atmospheric and sea ice conditions

The BH index for autumn (September, October, and November) 2018 was moderate, ranking the tenth highest in 1979–2018 (Fig. 3a). However, the BH index for the following winter (December, January, and February) was much lower at −5.6 hPa, ranking the fourth lowest in 1979–2018 (Fig. 3b). Both CAI and DA were positive in autumn 2018, but still within one standard deviation of 1979–2018 climatological values (Fig. 3c and 3e). In contrast to the BH index, both CAI and DA were strongly positive in winter 2018/19, ranking the third and second highest in 1979–2018, respectively (Fig. 3d and 3f). Sea ice in the PAO is expected to be impacted considerably by these seasonal changes in atmospheric circulation patterns as a result of the northward advection of sea ice to the Atlantic sector of the Arctic Ocean. As an example, extreme sea ice conditions have been observed in the Bering Sea in mid-March 2019, where sea ice extent was 70 %–80 % lower than normal (Perovich et al., 2019).

https://doi.org/10.5194/tc-2020-211
Preprint. Discussion started: 25 August 2020

Associated with the seasonal change in the BH index, there was a distinct contrast in the pattern of the BG between autumn and winter. Wind vectors and ice drift trajectories during autumn 2018 were generally clockwise, while those during the following winter were counterclockwise, with all buoys drifting northeastward from December 2018 onward and integrating into the TDS (Fig. 4). In autumn 2018, strong northerly winds only appeared in the northwestern part of study region (Fig. 4a), and were associated with moderately positive CAI and DA. However, in winter 2018/2019, enhanced northerly winds prevailed almost across the entire study region (Fig. 4b), and were associated with extremely positive CAI and DA. The T_{2m} anomalies averaged over the study region was 3.9 °C in autumn and 0.7 °C in winter (Fig. 4c and 4d), ranking the second and eleventh highest in 1979–2018, respectively. This can be attributed to the seasonality of Arctic Amplification as rapid ice growth in autumn results in a higher rate of temperature increase in autumn than in winter in the Arctic (Screen and Simmonds, 2010).

The CHINARE buoys were deployed within a narrow meridional section at about 170° W. On 20 August 2018, sea ice concentration in the northern part of this section was considerably higher than that in the southern part (Fig. 5a); sea ice concentration in this section was considerably lower than that in the eastern part of the study region at about 120° W where other buoys had been deployed. Subsequently, ice concentration increased considerably, with almost all buoys being located in the PIZ by 20 September 2018 (Fig. 5b). However, CHINARE buoys in the south and all T-ICE buoys remained within 70 km of the ice edge because it retreated further during August–September 2018. By 20 October 2018, ice concentration surrounding all buoys had increased to over 95 % (Fig. 5c).

In September and early October 2018, ice concentrations were considerably lower than the 1979–2018 average. Ice concentrations increased after early October and became comparable with climatological values (Figs. 6b and 7b). In October 2018, ice concentration was much lower in the southern and western parts of the study region than in the north and east. Subsequently, the spatial heterogeneity of sea ice concentration gradually decreased. Compared with 1979–2018 climatology, wind speed over the study period was low during most of the time except for episodic increases as a result of intrusions of low-pressure systems (Figs. 6c and 7c). The study region was dominated by low SLP during December 2018 and February 2019, which resulted in an anomalously low BH index and subsequent increases in both wind and ice drift speeds (Figs. 6c, 6d, 7c, and 7d). In September 2018, ice speed in the south was higher than that in the north (Fig. 6d), implying that sea ice response to wind forcing was stronger in the south because of lower ice concentration. From October 2018 onwards, this north–south difference gradually disappeared.

3.2 Sea ice kinematic characteristics

Temporal resampling has little effect on wind speed. However, applying longer resampling intervals to buoy position data may filter out ice motions at higher frequencies (Haller et al., 2014), resulting in reduced ice speed and IWSR (Fig. 8). For example, ice drift speed and IWSR in September 2018 were 0.13 m s^{-1} and 0.027 at a resampling interval of 1 h, and decreased to 0.01 m s^{-1} and 0.021 at a resampling interval of 48 h. Both ice speed and IWSR decreased considerably from September to November 2018; afterwards, values of both parameters remained low until the end of the study period. At a resampling interval of 6h, the IWSR was 0.026 in September 2018 (Fig. 8), which is much lower than that (0.013) obtained in the region close to North Pole in the same month of 2007 (Haller et al., 2014) because most parts of our study region involves MIZ. This value decreased to 0.008–0.015 during November to February (Fig. 8), which is comparable with those obtained from the regions north of Siberia or Greenland and the region close to North Pole during the freezing season, but much smaller than that obtained from Fram Strait (Haller et al., 2014). This implies that, during the freezing season, the response of sea ice to wind forcing is relatively uniform for the entire Arctic Ocean except for the strait regions where ice speed increases obviously. A more consolidated ice pack and relatively weak wind forcing as a result of the domination of a high-pressure system led to both ice drift speed and IWSR reaching minimums for the entire study period in January 2019 (Figs. 6c and 7c). Effect of resampling on IWSR was considerably reduced during the freezing season, implying remarkable reductions of meandering and sub-daily oscillations in ice motion during the freezing season. Ratio between IWSRs at 1-h and 48-h intervals in October was 70 % of that in September. This ratio remained almost unchanged between November and February.

Factors impacting IWSR are summarized in Table 1. Impact of geographical location was significant in autumn, resulting in relatively high IWSR values in the southern or western parts of the study region. However, impact of latitude became very slight in January–February because the north–south gradient in ice conditions was negligible by that time. The west–east gradient was more pronounced, resulting in a significant relationship between longitude and IWSR from autumn until February. This is consistent with the results given by Lukovich et al. (2011), who identified that the west–east gradient of sea ice

https://doi.org/10.5194/tc-2020-211
Preprint. Discussion started: 25 August 2020

motion is larger than that in the north–south direction for the south of PAO during the freezing season. In summer and early autumn, consolidation of the ice field is low, and interactions between ice floes approximate rigid particle collisions (Lewis and Richter-Menge, 1998). Thus, lower IWSR in August–October 2018 is related to stronger wind forcing that strengthened interactions between floes, leading to higher consumption of the kinetic energy of the ice field. Under the weak wind forcing, the inertial component of ice motion would increase and the IWSR would increase, which also lead to a significant statistical negative correlation between IWSR and wind speed. Similarly, based on the data obtained from the buoys deployed in the TDS region, Haller et al. (2014) also found that the spikes of the IWSR were associated with the low wind speed. Consolidation of the ice field between November and February 2018 resulted in reduced ice motion and weaker sea ice response to wind forcing. As a result, impact of wind forcing on IWSR was insignificant from November onwards. Variations of T_{2m} across the study region between 20 August and 30 September 2018 were relatively small (−1.7 to −3.5 °C) because of the thermodynamic equilibrium between sea ice and the atmosphere during the melt season (Screen and Simmonds, 2010). Thus, the statistical relationship between T_{2m} and the IWSR was insignificant during this period. However, the relationship became significant during October–December 2018, with higher T_{2m} being associated with higher IWSR because warmer conditions may have weakened ice pack consolidation (Oikkonen et al., 2017). As continued thickening of the ice cover further reduced the influence of air temperature on ice motion, the statistical relationship between T_{2m} and the IWSR was insignificant in January and February 2019.

The inertial oscillation of ice motion is stimulated by sudden changes in external forces, majorly due to enhanced wind forcing (Gimbert et al., 2012). It was weakened due to kinetic energy dissipation because of surface friction and internal ice stresses. Thus, inertial component of ice motion is closely associated with the seasonal and spatial changes in ice conditions. Figure 9 shows monthly IMI obtained from each buoy displayed at the midpoint of the buoy's trajectory for different months. Average IMI of all available buoys for the study period was 0.090±0.065, with the average for September 2018 (0.209) being considerably higher. Monthly average IMI from all buoys decreased from 0.108 in October 2018 to 0.035 in February 2019. Spatial variability of the IMI had almost disappeared by February 2019; IMI standard deviation in February 2019 was 12 %–20 % of that in September–October 2018. The analysis of inertial components of sea ice motion for the entire Arctic Ocean also reveals that their seasonal changes mainly occurs in seasonal ice region. On the contrary,

https://doi.org/10.5194/tc-2020-211
Preprint. Discussion started: 25 August 2020

that in the pack permanent ice region is almost negligible (Gimbert et al., 2012). To eliminate the influence of large-scale spatial variability, we inspected subsets of data obtained from buoys deployed in clusters. The IMI obtained from the CHINARE buoy cluster (black circles in Fig. 2) decreased markedly from 0.213 to 0.071 during September–October 2018. However, a similar change was observed one month later in October–November 2018 for the T-ICE buoy cluster. During the freezing season from November to February, the IMI gradually decreased to 0.036 for the CHINARE cluster and to 0.032 for the T-ICE cluster. Sea ice growth rate of the thin ice in the MIZ in the western and southern parts of the study region is expected to be higher than that in the PIZ in the north or the east (e.g., Kwok and Cunningham, 2008). Accordingly, the ice cover in the MIZ consolidated more rapidly than that in the PIZ, and the spatial variability of ice inertial oscillation observed in early autumn gradually disappeared.

3.3 Sea ice deformation

For all the buoy triangles used to estimate ice deformation, ice concentration within the CHINARE buoy cluster increased rapidly during late August and early September 2018, and remained close to 100 % from then onwards (Fig. 10a). However, a comparable seasonal increase in ice concentration within the T-ICE buoy cluster was observed one month later. To facilitate direct comparison of data obtained from two different years, we estimated ice deformation rate of the T-ICE buoy cluster at the 10–20 km scale using the value at the 40–80 km scale and a constant spatial scaling exponent of 0.55. The scaling exponent of 0.55 is a seasonal average obtained from the CHINARE buoy cluster. A change of the scaling exponent by 10 % would lead to an uncertainty of about 0.03 for the ice deformation rate. Thus, a change in the scaling exponent can be ignored in a study of seasonal variation, and a constant scaling exponent can be used. In early and mid-September 2018, ice deformation rate was low for the CHINARE cluster (Fig. 10b) because of low wind speed and infrequent changes in wind direction, and despite a weakly consolidated ice field (Fig. 2). For the T-ICE cluster, both ice deformation rate and ratio between ice deformation rate and wind speed decreased rapidly between 20 September and 10 November 2018, associated with consolidation of the ice field as ice concentration and thickness increased and temperature decreased. However, ice deformation rate from the CHINARE cluster decreased only slightly over the same period, which is likely because ice concentration in the CHINARE region in late September 2018 was higher than that in the T-ICE region by 15 %–20 %.

For the CHINARE buoy cluster, daily wind speed can explain 35 % (P<0.001) of the daily ice deformation rate estimated using hourly position data over the study period. However, for the T-ICE cluster between September and early November 2018, changes in ice deformation were mainly regulated by the seasonal evolution of ice concentration. Thus, the relationship between ice deformation rate and wind speed was insignificant at the statistical confidence level of 0.05 during this period. The ice field had sufficiently consolidated by mid-November 2018, and the relationship between daily ice deformation rate and daily wind speed changed to significant (R^2=0.12, P<0.01) from then onwards.

Average ratio of ice deformation rate to wind speed in autumn was 1.15×10^{-6} m^{-1} for the CHINARE cluster and 0.62×10^{-6} m^{-1} for the T-ICE cluster; the ratio in winter decreased to 0.86×10^{-6} and 0.17×10^{-6} m^{-1}. This is consistent with results of Spreen et al. (2017) by using the RGPS data, which showed that annual maximum ice deformation rate occurred in August, and decreased gradually to the annual minimum in March. Except for late September 2018, when ice concentration in the T-ICE cluster was less than 85 %, ice deformation rate from the CHINARE cluster was generally larger than that from the T-ICE cluster, with average values of 0.45 and 0.13 d^{-1}, respectively, for October 2018 to February 2019. Sea ice in the region of the T-ICE cluster was generally thinner than that in the region of the CHINARE cluster. Thus, difference in ice deformation rate cannot be explained by difference between ice conditions in the two regions, and is most likely attributed to spatial heterogeneity and temporal variability of wind and/or oceanic forcing. The CHINARE cluster was located in the core region of the BG; thus, vorticity of the surface current must be greater than that in the T-ICE cluster, which was located at the western boundary of the BG (Armitage et al., 2017). Furthermore, changes in the direction of wind vectors were more frequent around the CHINARE cluster than around the T-ICE cluster. Frequent changes in ice drift direction lead to larger ice deformation, such as the events on 11 October, and 11 and 26 November 2018 for the CHINARE cluster shown in Fig. 10b. Drifting trajectory of the T-ICE cluster was much straighter than that of the CHINARE cluster. As a result, ice deformation rate and its ratio to wind speed were lower for the T-ICE cluster than for CHINARE cluster.

Ice deformation rates obtained from the CHINARE buoy cluster at three representative lengths of 7.5, 15, and 30 km were estimated using Eq. (6). Influence of synoptic processes, e.g., cyclonic activities and/or changes in wind direction, was filtered out by using a monthly window. Figure 11 shows that monthly average ice deformation decreased as length scale and resampling interval increased, implying ice deformation localization and intermittency. Ice deformation decreased rapidly at all spatial and temporal scales during the seasonal transition period of September–October, and remained low from then onwards. Ice deformation rate obtained from hourly position data from the CHINARE buoy cluster in September 2018 was 0.38 d^{-1} at the length scale of 30 km, which is comparable with that in September 2016 (0.31 d^{-1}), and much larger than that in September 2014 (0.18 d^{-1}) observed also in northern PAO (Lei et al., 2020b). These observed differences can be attributed to the strong storms in late September 2018 (Fig. 10b) and early September 2016 (Lei et al., 2020b), as well as the relatively stable synoptic conditions and relatively compact ice conditions in September 2014 (Lei et al., 2020b).

The spatial scaling exponent β from hourly position data was 0.61 in September 2018, and is comparable with that from September 2016 (0.60), but slightly larger than that in September 2014 (0.46) observed in northern PAO (Lei et al., 2020b). This can be attributed to similar ice conditions in September 2016 and 2018, and a more compact ice cover in September 2014. In late August 2018, ice concentration was about 85 % in the CHINARE buoy cluster (Fig. 10a), which is comparable to that (80 %) in 2016, but much lower than that in 2014 (96 %) (Lei et al., 2020b). The value of β decreased markedly from September to October 2018, and varied little from then onwards (Fig. 12). With increases in ice thickness and concentration and cooling of the ice cover, consolidation of the ice field is enhanced, and sea ice deformation can spread over longer distances from October onwards. By February 2019, the spatial scaling exponent β from hourly position data decreased to 0.48, which is comparable with that (0.43) obtained from February 2015 in the northern PAO (Lei et al., 2020a). This imply the year-to-year changes in the spatial scaling of ice deformation during winter is not strong as that in early autumn, which is similar with the change pattern of ice thickness (e.g., Kwok and Cunningham, 2008). The value of β decreased exponentially with increase in sampling frequency for all months, which indicates the spatial scaling would be underestimated with the coarsened observation temporal resolution.

The temporal scaling exponent α also exhibited a strong dependence on spatial scale (Fig. 13). The value of α decreased between September and October 2018 because of enhanced consolidation of the ice cover. The value of the space–time coupling coefficient c increased monotonously from 0.034 in autumn to 0.062 in winter, suggesting gradual enhancement of the brittle rheology of the ice cover. The value of *c* in September 2018 is comparable with that in September 2016 (0.03). However, it is only about half that in September 2014 (0.06) (Lei et al., 2020b). The value of *c* in January–February 2019 (0.059–0.062) is comparable with the values obtained in September 2014 (0.050) and in January–February 2015 (0.051–0.077) from the northern PAO (Lei et al., 2020a), and the value obtained for the region north of Svalbard in winter and spring (Oikkonen et al., 2017), indicating that sea ice compactness in the northern PAO in September 2014 was comparable with that in winter.

The areal localization index denotes the area with the highest deformation. It had a strong dependence on temporal scale, and increased linearly as logarithm of the temporal scale increased (Fig. 14), which implies that the localization of ice deformation would be underestimated by the observations or models with coarse resolution. Areal localization index decreased markedly from September to November 2018, indicating that ice deformation was increasingly localized during the transition from melt to freezing. However, degree of deformation strongly regulated localization of ice deformation, with monthly ice deformation rate explaining 96 % of the monthly areal localization index ($P<0.01$) during November–February. This means that extremely high ice deformation can spread over longer distances. Areal localization index for January–February 2019 corresponding to temporal resolution of 1 h and length scale of 10–20 km was 1.9 %–2.3 %, which was close to the value (2.4 %–2.7 %) estimated at the length scale of 18 km using a high resolution numerical model (Spreen et al., 2017).

4 Discussions

High intermittence of ice deformation implies that episodic opening or closing of the sea ice cover may be undetectable in data with longer sampling intervals, such as remote sensing data with temporal resolutions of one or two days. Consequently, fluxes of heat (e.g., Heil and Hibler, 2002) or particles and gases (e.g., Held et al., 2011) released from the openings to the atmosphere would be underestimated if they are derived from remote sensing products, highlighting the importance of using data with higher resolution to characterize sea ice deformation accurately. Our results also show that ice deformation intermittence is underestimated at longer spatial scales. This is consistent with results from numerical models, which indicate that the most extreme deformation events may be absent in the output of models with lower spatial resolution (Rampal et al., 2019), emphasizing the need for high-resolution sea ice dynamic models to reproduce linear kinematic features of ice deformation (e.g., Hutter and Losch, 2020). Dependence of the ratio of ice speed to wind speed on resampling frequency implies that temporal resolution should be considered carefully when using wind forcing data to parameterize or simulate sea ice drift (e.g., Shu et al., 2012).

The PAO is the region with the most significant summer sea ice loss across the entire Arctic Ocean (Comiso et al., 2017). Summer ice conditions have profound effects on sea ice dynamic and thermodynamic processes in the following winters. Enhanced divergence of summer sea ice leads to increased solar radiation absorption by the upper ocean and delays onset of ice growth (e.g., Lei et al., 2020b). Our results indicate that an increase in open water fraction in summer would have a considerable effect on the kinematic and deformation characteristics of sea ice in autumn and winter. Pronounced loss of sea ice in the southern and western parts of the study region resulted in an inertial signal and ice motion response to wind forcing that were stronger than those found to the north and the east. As shown in Fig. 15, the long-term decrease of sea ice concentration in the first half of September, when Arctic sea ice extent reaches its annual minimum (Comiso et al., 2017), is more obvious and significant in the southern and western parts of the study region than in the north and the east. The western and southern parts of the study region have become ice free in September during some years recently. On the contrary, there is no significant trend in ice concentration in the first half of September along the trajectory of the easternmost buoy (Fig. 15e). This implies that as sea ice loss continues in the western and southern parts of the study region, north–south and east–west differences in sea ice kinematics are likely to be enhanced.

Multi-year ice in the Pacific and eastern sectors of the Arctic Ocean is being depleted gradually (Serreze and Meier, 2018), resulting in the domination of seasonal ice. Consequently, a deformation of the ice field creates unfrozen first-year ice ridges (Salganik et al., 2020). These new ridge areas, together with the newly formed thin ice area in leads, are mechanically vulnerable parts of the ice field, and predispose the ice field to further deformation under external forces. The ongoing ice drifting station of the international Multidisciplinary drifting Observatory for the Study of Arctic Climate (MOSAiC) has been designed to operate for a year (2019–2020) from the region north of the Laptev Sea, at 136° E, 85° N (Krumpen et al., 2020), which is to the west of the area of the T-ICE buoy cluster. Ice thickness around the MOSAiC ice station is much lower (Krumpen et al., 2020) than that in

https://doi.org/10.5194/tc-2020-211
Preprint. Discussion started: 25 August 2020

The Cryosphere Discussions
Open Access
EGU

the areas of the buoy clusters included in this study. Frequent sea ice breaking has been observed around the central observatory of MOSAiC during the drifting. Thus, data and results from this study can be used as a proxy baseline for comparing and investigating deformation of the MOSAiC ice pack.

In this study, we examined atmospheric influences on sea ice kinematics and deformation. The ocean also plays an important role on ice drift and deformation, especially at mesoscales, greatly enhancing ice motion nonuniformity and ice deformation (e.g., Zhang et al., 1999). In the PAO, mesoscale ocean eddies prevail over the shelf break and the Northwind and Alpha-Mendeleyev Ridges (e.g., Zhang et al., 1999, Zhao et al., 2016). To characterize the influence of mesoscale oceanic eddies on ice deformation, observations from ice-drifter arrays are insufficient, highlighting the need to combine deployment of ocean-profiler arrays as part of the distributed network of MOSAiC (Krumpen et al., 2020).

5 Conclusion

High-resolution position data measured by 32 ice-based drifting buoys in the PAO between August 2018 and February 2019 were analyzed in detail to characterize spatiotemporal variations of sea ice kinematic and deformation properties during autumn–winter of the 2018/19 ice season. Our results show that there was a distinct change in the circulation of the BG during the transition from autumn to winter, which is most likely a result of the intrusion of a low-pressure system into the western Arctic Ocean. Furthermore, enhanced positive phases of the CAI and DA resulted in a considerable increase in northerly winds in winter relative to autumn. Because of seasonal change in the large-scale atmospheric circulation pattern, a clear change in ice drift direction was observed in late November 2018, leading to temporal increases in both ice deformation rate and its ratio to wind forcing.

During the transition from autumn to winter, ice deformation rate, ratio between deformation rate and wind speed, and the inertial signal of ice motion gradually weakened. At the same time, space–time coupling of ice deformation increased as the mechanical strength of the ice field increased. During the freezing season between October 2018 and February 2019, ice deformation rate in the northern part of the study region was about 2.5 times that in the western part. We attribute this difference to the higher spatial heterogeneity of oceanic and atmospheric forcing in the northern part of the study region, which is in the core region of the BG, relative to the western part.

The response of ice kinematics to wind and inertia forcing was stronger in the south and west than in the north and east of the study region, which is partly associated with the spatial heterogeneity of ice conditions inherited from previous seasons. During the transition from autumn to winter, the north–south and east–west gradients in IWSR and inertial component of ice motion gradually decreased and even disappeared entirely, which is in line with the seasonal evolution of ice concentration and thickness. Spatial heterogeneity in ice concentration and ice motion in autumn is likely to be amplified with further increased loss of summer ice cover in the southern and western parts of PAO.

Author contributions

RL conceived the study and wrote the paper. MH, BC, GZ, and GD undertook the processing and analysis of the buoy data, and interpretation of results. RL, WY, and JB deployed the buoys. The buoy data were provided by RL, MH, and BC. The calculation of atmospheric circulation index was done by QC. All authors commented on the manuscript.

Data availability

The CHINARE buoy data are archived in the National Arctic and Antarctic Data Centre of China at https://www.chinare.org.cn/metadata/53de02c5-4524-4be4-b7bb-b56386f1341c (DOI: 10.11856/NNS.D.2020.038.v0). The T-ICE buoy data were initially archived in the online sea-ice knowledge and data platform at www.meereisportal.de, and will be available in the data repository PANGAEA finally. The IABP buoy data are archived at http://iabp.apl.washington.edu/index.html.

Competing interests

The authors declare that they have no conflict of interest.

Acknowledgments

We are most grateful to the Chinese Arctic and Antarctic Administration and the Alfred-Wegener-Institute for their logistical and financial support of the cruises of CHINARE and T-ICE, respectively. We thank the captains, crews and science parties of the R/V Xuelong and the Akademik Tryoshnikov, especially cruise leaders Dr. Zexun Wei and Dr. Benjamin Rabe, for their incredible support during the expeditions. The AMSR2 passive microwave ice concentrations were provided by the University of Bremen. The SMMR-SSMIS ice concentration and ice motion products, and the monthly Arctic Sea Ice Index were provided by the NSIDC. The ERA-Interim reanalysis was obtained from the ECMWF. Monthly sea level pressure is obtained from the NCEP/NCAR reanalysis I dataset.

Financial support

This work was supported by grants from the National Key Research and Development Program (2018YFA0605903, 2016YFC1400303 and 2016YFC1401800) and the National Natural Science Foundation of China (41722605 and 41976219). B.C. was supported by the European Union's Horizon 2020 research and innovation programme (727890 – INTAROS) and Academy of Finland under contract 317999. The buoys deployed on T-ICE were funded by the Alfred-Wegener-Institute through the infrastructure programs FRAM and ACROSS.

References

Alam, A. and Curry, J. A.: Evolution of new ice and turbulent fluxes over freezing winter leads, J. Geophys. Res. Oceans, 103, 15783–15802, 1998.

Armitage, T. W. K., Bacon, S., Ridout, A. L., Petty, A. A., Wolbach, S., and Tsamados, M.: Arctic Ocean surface geostrophic circulation 2003–2014, The Cryosphere, 11, 1767–1780, https://doi.org/10.5194/tc-11-1767-2017, 2017.

Assmy, P., Fernández-Méndez, M., Duarte, P., and other coauthors: Leads in Arctic pack ice enable early phytoplankton blooms below snow-covered sea ice, Sci. Rep., 7:40850. https://doi.org/10.1038/srep40850, 2017.

Comiso, J. C., Meier, W. N., and Gersten, R.: Variability and trends in the Arctic sea ice cover: results from different techniques, J. Geophys. Res. Oceans, 122, 6883–6900, doi:10.1002/2017JC012768, , 2017.

Dee, D. P., Uppala, S. M., Simmons, A. J., et al.: The ERA-interim reanalysis: configuration and performance of the data assimilation system, Quarterly Journal of the Royal Meteorological Society, 137, 553–597. https://doi.org/10. 1002/qj.828, 2011.

https://doi.org/10.5194/tc-2020-211
Preprint. Discussion started: 25 August 2020

Fetterer, F., Knowles, K., Meier, W. N., Savoie, M., and Windnagel, A. K.: Updated daily sea ice index, version 3, sea ice concentration, Boulder, Colorado USA. NSIDC: National Snow and Ice Data Center. doi: https://doi.org/10.7265/N5K072F8, 2017.

Fernández-Méndez, M., Olsen, L. M., Kauko, H. M., and other coauthors: Algal hot spots in a changing Arctic Ocean: sea-ice ridges and the snow-ice interface, Front Mar. Sci., 5: 75. https://doi.org/10.3389/fmars.2018.00075, 2018.

Fowler, C., Emery, W., and Tschudi, M.: Polar Pathfinder daily 25 km EASE-Grid sea ice motion vectors, version 2., edited. Boulder, Colorado USA: National Snow and Ice Data Center, 2013.

Gimbert, F., Marsan, D., Weiss, J., Jourdain, N. C., and Barnier, B.: Sea ice inertial oscillations in the Arctic Basin, The Cryosphere, 6, 1187–1201, 2012.

Haller, M., Brümmer, B., and Müller, G.: Atmosphere–ice forcing in the transpolar drift stream: results from the DAMOCLES ice-buoy campaigns 2007–2009, the Cryosphere, 8, 275–288, 2014.

Heil, P., and Hibler III, W. D.: Modeling the high-frequency component of Arctic sea ice drift and deformation, J. Phys. Oceanogr., 32, 3039–3057, 2002.

Held, A., Brooks, I. M., Leck, C., and Tjernström M.: On the potential contribution of open lead particle emissions to the central Arctic aerosol concentration, Atmos. Chem. Phys., 11, 3093–3105, https://doi.org/10.5194/acp-11-3093-2011, 2011.

Herman, A., and Glowacki, O.: Variability of sea ice deformation rates in the Arctic and their relationship with basin-scale wind forcing, The Cryosphere, 6(6), 1553–1559, doi:10.5194/tc-6-1553-2012, 2012.

Hutchings, J. K., and Hibler III, W. D.: Small-scale sea ice deformation in the Beaufort Sea seasonal ice zone, J. Geophys. Res., 113, C08032, doi:10.1029/2006JC003971, 2008.

Hutchings, J. K., Heil, P., Steer, A., and Hibler III, W. D.: Subsynoptic scale spatial variability of sea ice deformation in the western Weddell Sea during early summer, J. Geophys. Res., 117, C01002, doi:10.1029/2011JC006961, 2012.

Hutter, N., Losch, M., and Menemenlis, D.: Scaling properties of arctic sea ice deformation in a high-resolution viscous-plastic sea ice model and in satellite observations, J. Geophys. Res. Oceans, 123, 672–687, https://doi.org/10.1002/2017JC013119, 2018.

Hutter, N., and Losch, M.: Feature-based comparison of sea ice deformation in lead-permitting sea ice simulations, The Cryosphere, 14, 93–113, https://doi.org/10.5194/tc-14-93-2020, 2020.

Itkin, P., Spreen, G., Hvidegaard, S. M., Skourup, H., Wilkinson, J., Gerland, S., and Granskog, M. A.: Contribution of deformation to sea ice mass balance: A case study from an N-ICE2015 storm, Geophys. Res. Lett., 45, 789–796, https://doi.org/10.1002/2017GL076056, 2018.

Krumpen, T., Birrien, F., Kauker, F., and other coauthors: The MOSAiC ice floe: sediment-laden survivor from the Siberian shelf, The Cryosphere, 14, 2173–2187, https://doi.org/10.5194/tc-14-2173-2020, 2020.

Kwok, R.: Contrasts in sea ice deformation and production in the Arctic seasonal and perennial ice zones, J. Geophys. Res., 111, C11S22, doi:10.1029/2005JC003246, 2006.

Kwok, R., and Cunningham, G. F.: ICESat over Arctic sea ice: Estimation of snow depth and ice thickness, J. Geophys. Res., 113, C08010, doi:10.1029/2008JC004753, 2008.

Lei, R., Tian-Kunze, X., Leppäranta, M., Wang, J., Kaleschke, L., and Zhang Z.: Changes in summer sea ice, albedo, and portioning of surface solar radiation in the Pacific sector of Arctic Ocean during 1982–2009, J. Geophys. Res. Oceans, 121, 5470–5486, doi:10.1002/2016JC011831, 2016.

Lei, R., Gui, D., Hutchings, J. K., Wang, J., Pang X.: Backward and forward drift trajectories of sea ice in the northwestern Arctic Ocean in response to changing atmospheric circulation. Int. J. Climatol., 1–20. DOI: 10.1002/joc.6080, 2019.

Lei, R., Gui, D., Hutchings, J. K., Heil, P., Li, N.: Annual cycles of sea ice motion and deformation derived from buoy measurements in the western Arctic Ocean over two ice seasons. J. Geophys. Res., 125, e2019JC015310, https://doi.org/10.1029/2019JC015310, 2020a.

Lei, R., Gui, D., Heil, P., Hutchings, J.K., Ding, M.: Comparisons of sea ice motion and deformation, and their responses to ice conditions and cyclonic activity in the western Arctic Ocean between two summers, Cold Reg. Sci. Technol., 170, 102925, https://doi.org/10.1016/j.coldregions.2019.102925, 2020b.

Lewis, J. K., and Richter-Menge, J. A.: Motion-induced stresses in pack ice, J. Geophys. Res., 103(C10), 21831– 21843, doi:10.1029/98JC01262, 1998.

Lindell, D. B., and Long, D. G.: Multiyear Arctic ice classification using ASCAT and SSMIS. Remote Sens., 8, 294; doi:10.3390/rs8040294, 2016.

Lüpkes, C., Vihma, T., Birnbaum, G., and Wacker, U.: Influence of leads in sea ice on the temperature of the atmospheric boundary layer during polar night, Geophys. Res. Lett., 35, L03805, https://doi.org/10.1029/2007GL032461, 2008.

Lukovich, J. V., Babb, D. G., and Barber D. G.: On the scaling laws derived from ice beacon trajectories in the southern Beaufort Sea during the International Polar Year-Circumpolar Flaw Lead study, 2007–2008, J. Geophys. Res., 116, C00G07, doi:10.1029/2011JC007049, 2011.

Marsan, D., Stern, H., Lindsay, R., and Weiss, J.: Scale dependence and localization of the deformation of Arctic sea ice, Phys. Res. Lett., 93, 17, 178501, doi:10.1103/PhysRevLett.93.178501, 2004.

Marsan, D., and Weiss, J.: Space/time coupling in brittle deformation at geophysical scales, Earth Planet Sci. Lett., 296(3–4), 353–359, 2010.

Moore, G. W. K., Schweiger, A., Zhang, J., and Steele, M.: Collapse of the 2017 winter Beaufort High: A response to thinning sea ice? Geophys. Res. Lett., 45: 2860–2869. https://doi.org/10.1002/2017GL076446, 2018.

Oikkonen, A., Haapala, J., Lensu, M., Karvonen, J., and Itkin, P.: Small-scale sea ice deformation during N-ICE2015: From compact pack ice to marginal ice zone, J. Geophys. Res. Oceans, 122, 5105–5120, doi:10.1002/2016JC012387, 2017.

Perovich, D., Meier, W., Tschudi, M., Farrell, S, Hendricks, S., Gerland, S., Kaleschke, L., Ricker, R., Tian-Kunze, X., Webster, M., and Wood, K.: Sea ice. Arctic report card 2019, 26–34, http://www.arctic.noaa.gov/Report-Card, 2019.

Proshutinsky, A., Krishfield, R., Timmermans, M. L., Toole, J., Carmack, E., McLaughlin, F., Williams, W. J., Zimmermann, S., Itoh, M., and Shimada, K.: Beaufort Gyre freshwater reservoir: State and variability from observations. J. Geophys. Res., 114, C00A10, doi:10.1029/2008JC005104, 2009.

Rampal, P., Weiss, J., Marsan, D., Lindsay, R., and Stern, H.: Scaling properties of sea ice deformation from buoy dispersion analysis. J. Geophys. Res., 113, C03002, doi:10.1029/2007JC004143, 2008.

Rampal, P., Dansereau, V., Olason, E., Bouillon, S., Williams, T., Korosov, A., and Samaké, A.: On the multi-fractal scaling properties of sea ice deformation Article, Cryosphere, 13(9), 2457–2474, 2019.

Salganik, E., Høyland, K. V., and Maus, S.: Consolidation of fresh ice ridges for different scales. Cold Reg. Sci. Technol., 171, 102959, https://doi.org/10.1016/j.coldregions.2019.102959, 2020.

Screen, J. A., Simmonds, I.: Increasing fall-winter energy loss from the Arctic Ocean and its role in Arctic temperature amplification, Geophys. Res. Lett., 37, L16707, doi:10.1029/2010GL044136, 2010.

Serreze, M. C., Barry, R.G.: Processes and impacts of Arctic amplification: a research synthesis. Glob. Planet. Change., 77, 85–96, 2011.

https://doi.org/10.5194/tc-2020-211
Preprint. Discussion started: 25 August 2020

Serreze, M. C., and Meier, W. N.: The Arctic's sea ice cover: trends, variability, predictability, and comparisons to the Antarctic. Ann. N. Y. Acad. Sci., doi:10.1111/nyas.13856, 2018.

Shu, Q., Ma, H. and Qiao, F.: Observation and simulation of a floe drift near the North Pole. Ocean Dynamics, 62(8), 1195–1200, https://doi.org/10.1007/s10236-012-0554-4, 2012.

Spreen, G., Kwok, R., and Menemenlis, D.: Trends in Arctic sea ice drift and role of wind forcing: 1992–2009, Geophys. Res. Lett., 38: L19501, doi: 10.1029/2011GL048970, 2011.

Spreen, G., Kaleschke, L., and Heygster, G.: Sea ice remote sensing using AMSR-E 89 GHz channels J. Geophys. Res.,vol. 113, C02S03, doi:10.1029/2005JC003384, 2008.

Spreen, G., Kwok, R., Menemenlis, D., and Nguyen, A. T.: Sea-ice deformation in a coupled ocean–sea-ice model and in satellite remote sensing data, The Cryosphere, 11, 1553–1573, https://doi.org/10.5194/tc-11-1553-2017, 2017.

Steele, M., and Dickinson, S.: The phenology of Arctic Ocean surface warming, J. Geophys. Res. Oceans, 121, 6847–6861, doi:10.1002/2016JC012089, 2016.

Stern, H. L., and Lindsay, R. W.: Spatial scaling of Arctic sea ice deformation, J. Geophys. Res., 114, C10017, doi:10.1029/2009JC005380, 2009.

Strong, C., and Rigor, I. G.: Arctic marginal ice zone trending wider in summer and narrower in winter, Geophys. Res. Lett., 40, 4864–4868, doi:10.1002/grl.50928, 2013.

Vihma, T., Tisler, P., Uotila, P.: Atmospheric forcing on the drift of Arctic sea ice in 1989–2009, Geophys. Res. Lett. 39: L02501, doi: http://dx.doi.org/10.1029/2011GL050118, 2012.

Wang, J., Zhang, J., Watanabe, E., Mizobata, K., Ikeda, M., Walsh, J. E., Bai, X., Wu, B.: Is the Dipole Anomaly a major driver to record lows in the Arctic sea ice extent? Geophys. Res. Lett. 36: L05706. doi:10.1029/2008GL036706, 2009.

Woodgate, R. A., Weingartner, T. J., and Lindsay, R.: Observed increases in Bering Strait oceanic fluxes from the Pacific to the Arctic from 2001 to 2011 and their impacts on the Arctic Ocean water column. Geophys. Res. Lett., 39, L24603, doi:10.1029/2012GL054092, 2012.

Zhang, Y., Maslowski, W., and Semtner, A. J.: Impact of mesoscale ocean currents on sea ice in high-resolution Arctic ice and ocean simulations, J. Geophys. Res., 104(C8),18409–18429, doi:10.1029/1999JC900158, 1999.

Zhao, M., Timmermans, M.-L., Cole, S., Krishfield, R., and Toole, J.: Evolution of the eddy field in the Arctic Ocean's Canada Basin, 2005–2015, Geophys. Res. Lett., 43, 8106–8114, doi:10.1002/2016GL069671, 2016.

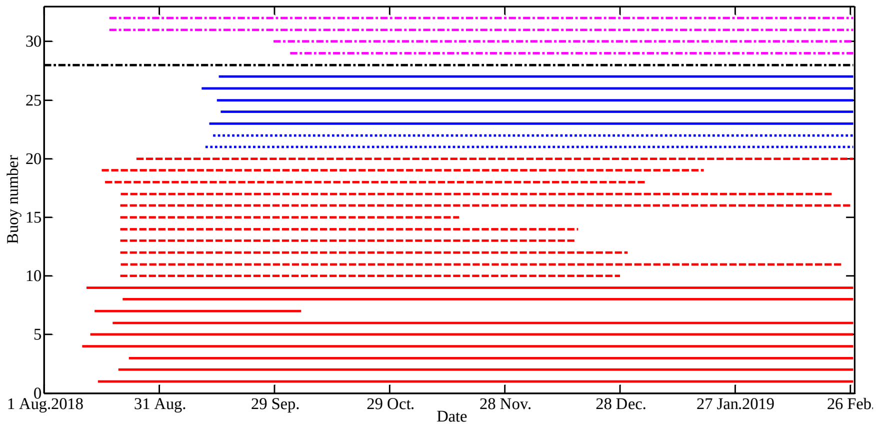

Figure 1 Operational periods of all buoys included in this study. Red lines denote buoys deployed during CHINARE in August 2018; blue lines denote buoys deployed during T-ICE; black line indicates the buoy deployed during CHINARE 2016; purple lines represent IABP buoys. Solid, dashed, short-dashed, and dot-dashed lines denote SIMBA, TUT, SB, and iSVP or other buoys, respectively.

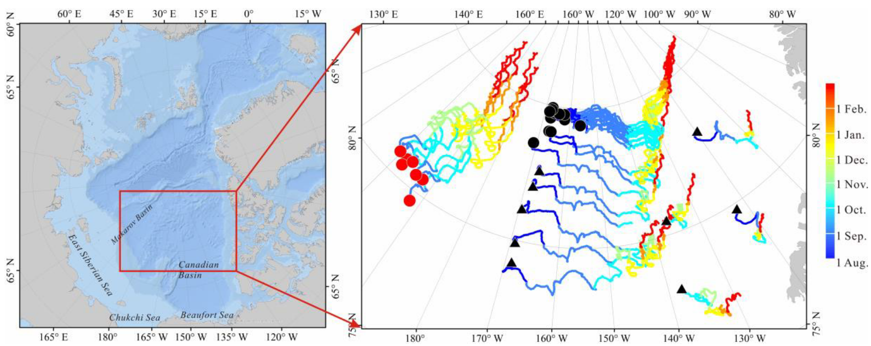

Figure 2 Buoy trajectories between deployment sites (indicated by circles and triangles) and buoy locations on 28 February 2019 at the end of the study period. Trajectories from 15 buoys deployed during CHINARE (at locations indicated by black circles) and 7 buoys deployed during T-ICE (at locations indicated by red circles) were used to estimate ice deformation rate. For buoys deployed prior to August 2018, the starting point of the trajectory was set to 1 August 2018.

https://doi.org/10.5194/tc-2020-211
Preprint. Discussion started: 25 August 2020

The Cryosphere Discussions
Open Access
EGU

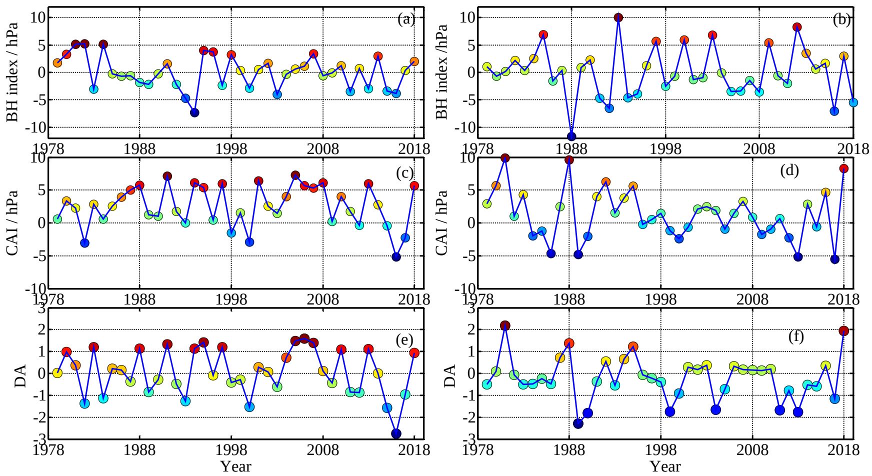

Figure 3 Changes in (a) autumn (SON) and (b) winter (DJF) BH index, (c) autumn and (d) winter CAI, and (e) autumn and (f) winter DA from 1979 to 2018.

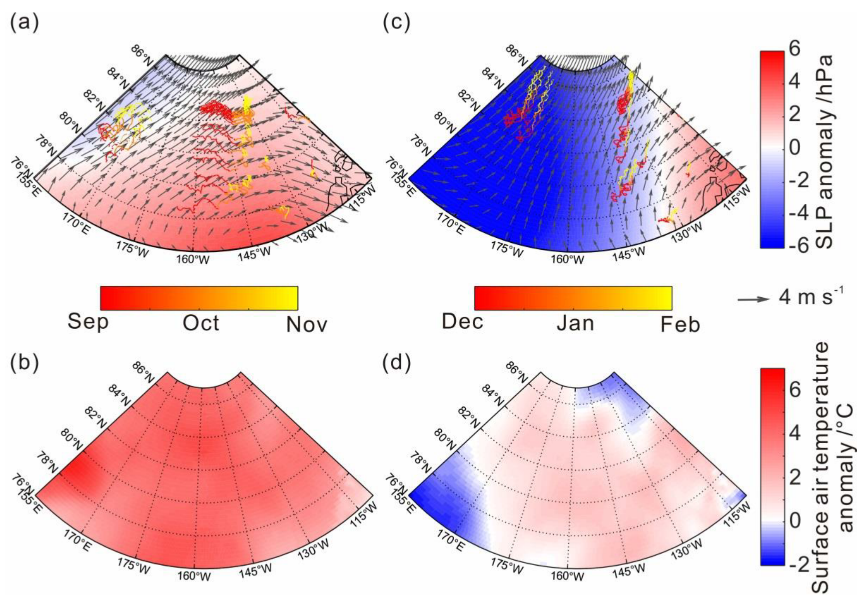

Figure 4 Anomalies of (a and c) SLP and (b and d) near-surface air temperature (2 m) over the PAO during (a and b) autumn 2018 and (c and d) winter 2018/19 relative to 1979–2018 climatology; (a and c) arrows indicate seasonal average wind vectors and colored lines indicate buoy trajectories through time.

https://doi.org/10.5194/tc-2020-211
Preprint. Discussion started: 25 August 2020

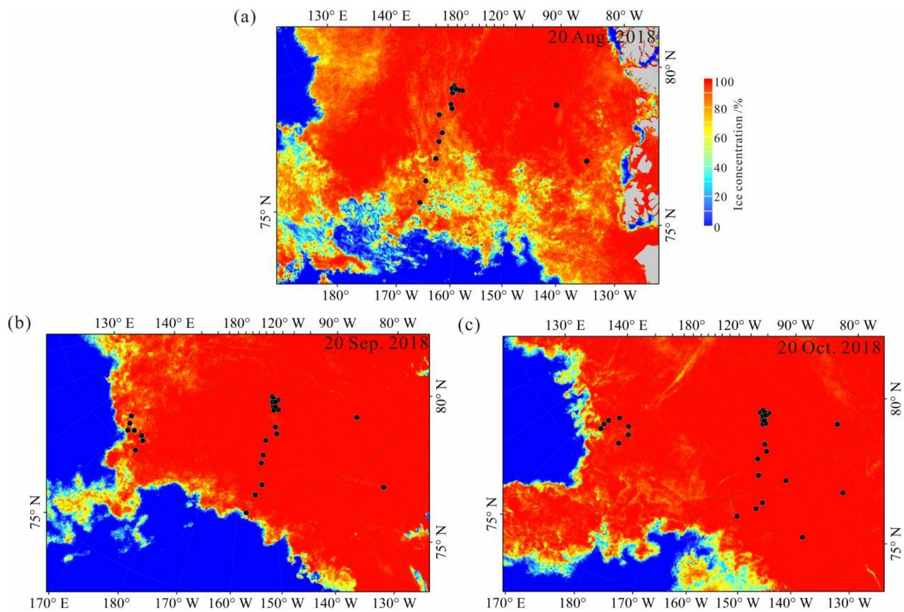

Figure 5 Sea ice concentration across the western Arctic Ocean on 20 of (a) August, (b) September, and (c) October, 2018, with black dots denoting buoy positions on the given days.

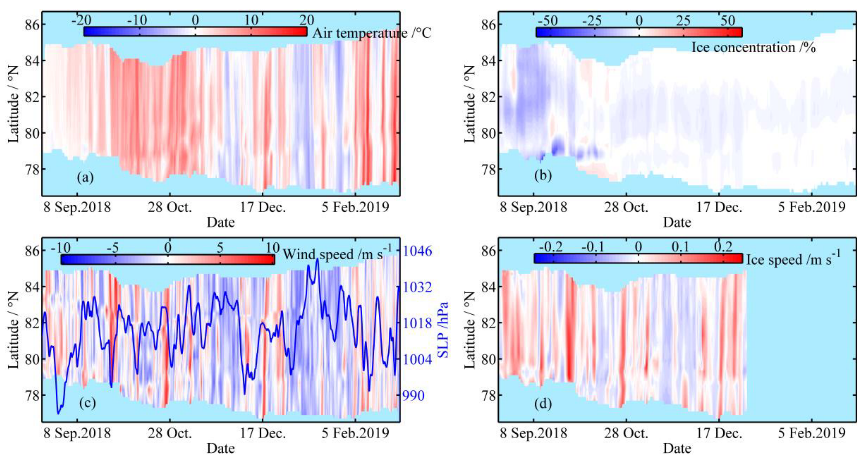

Figure 6 Meridional and temporal changes in anomalies of (a) T_{2m}, (b) ice concentration, (c) wind speed, (d) ice speed in the ice season 2018/19 relative to 1979–2018 climatology; (c) blue line indicates SLP averaged over the study region.

https://doi.org/10.5194/tc-2020-211
Preprint. Discussion started: 25 August 2020

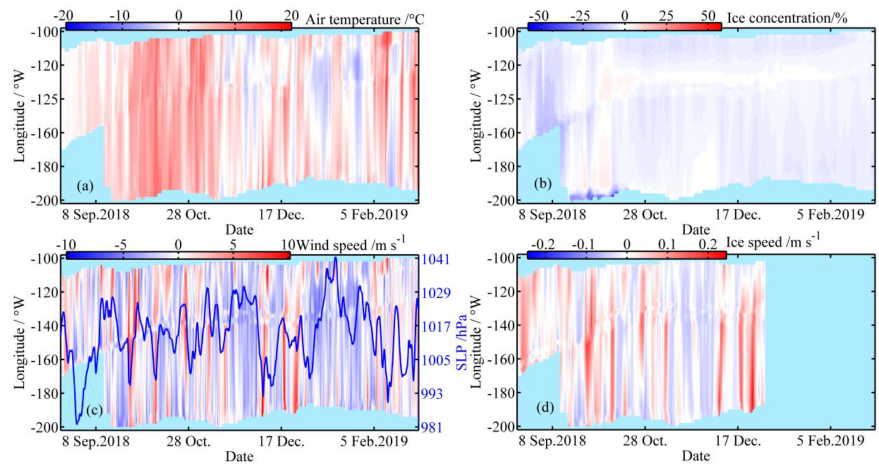

Figure 7 Same as Fig 2, but for zonal changes. Longitudes with values below −180 denote the eastern Arctic.

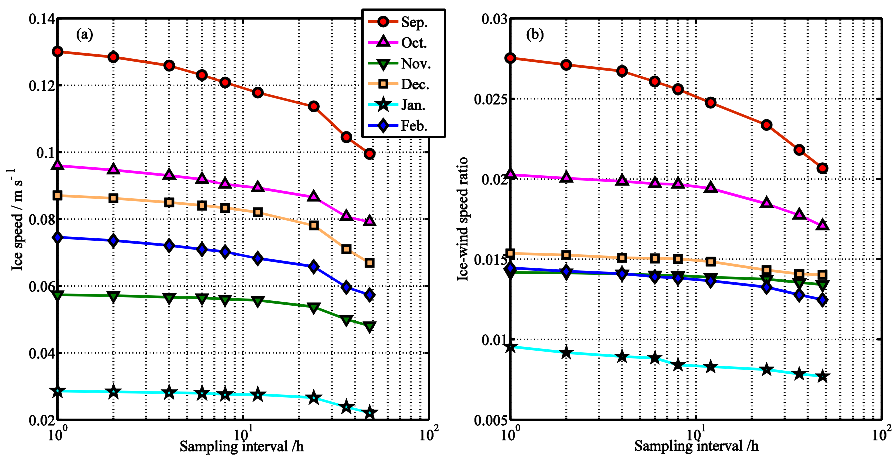

Figure 8 Changes in (a) ice speed and (b) IWSR as a function of position data resampling interval for various months in 2018/19.

https://doi.org/10.5194/tc-2020-211
Preprint. Discussion started: 25 August 2020

The Cryosphere
Discussions
Open Access

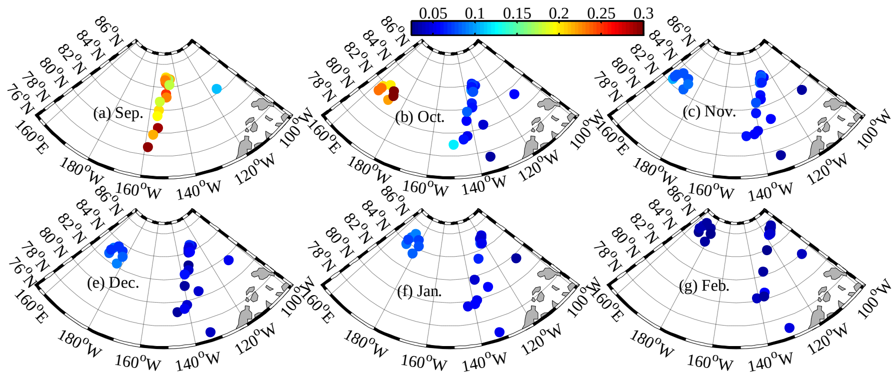

Figure 9 Amplitudes after Fourier transformation of monthly time series of normalized ice velocity at the inertial frequency from September 2018 to February 2019.

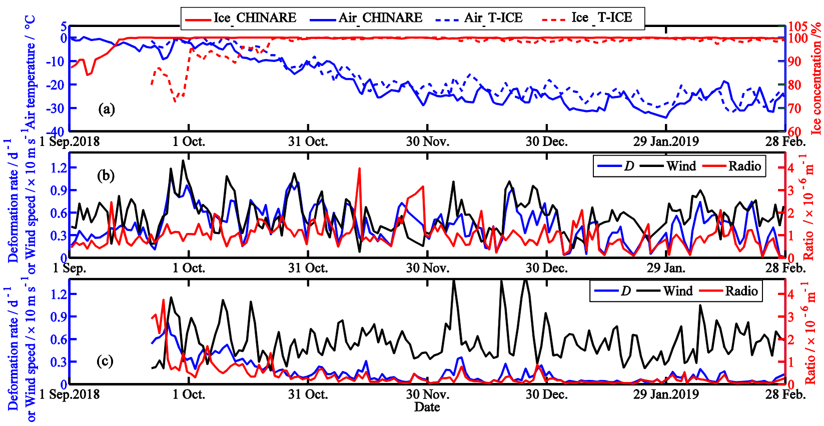

Figure 10 (a) Time series of daily average near-surface (2 m) air temperature and sea ice concentration within the CHINARE and T-ICE buoy clusters. Ice deformation rate (*D*), wind speed and their ratio at the 10–20 km scale for the (b) CHINARE and (c) T-ICE buoy clusters.

https://doi.org/10.5194/tc-2020-211
Preprint. Discussion started: 25 August 2020

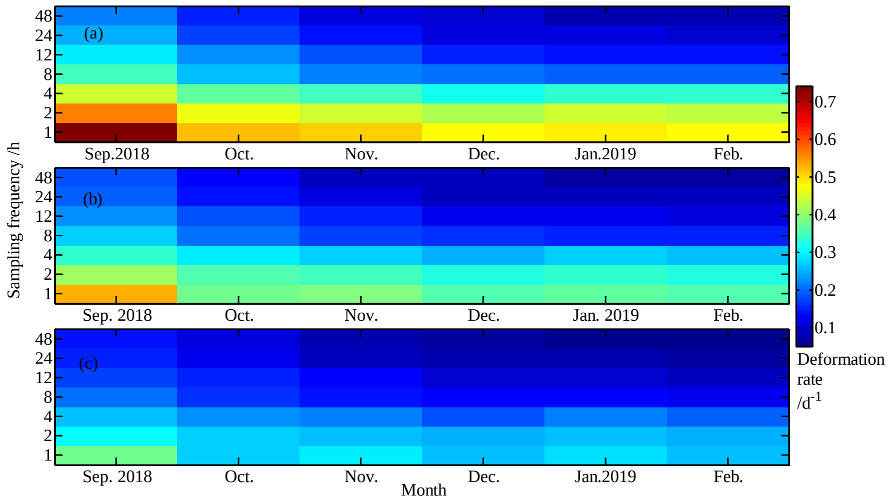

Figure 11 Monthly average sea ice deformation rate calculated from the CHINARE buoy cluster at length scales of (a) 7.5 km, (b) 15 km, and (c) 30 km using position data resampled at various intervals between 1 and 48 h.

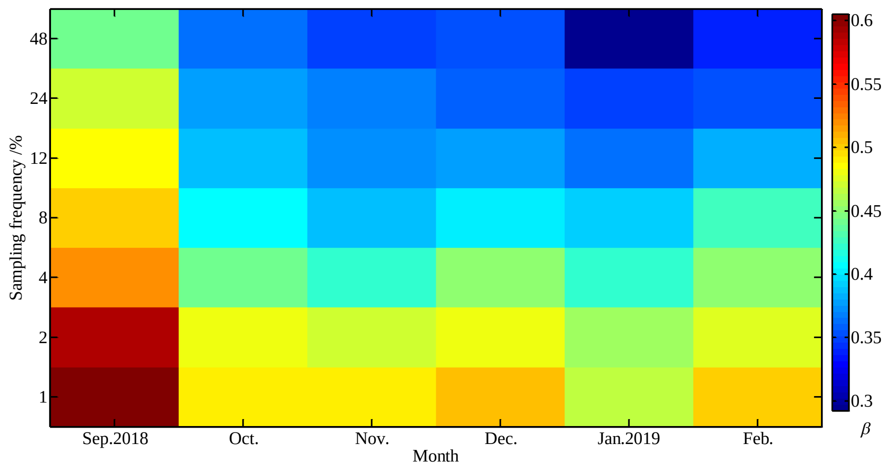

Figure 12 Changes in monthly spatial scaling exponent as a function of position data resampling frequency obtained from the CHINARE buoy cluster.

https://doi.org/10.5194/tc-2020-211
Preprint. Discussion started: 25 August 2020

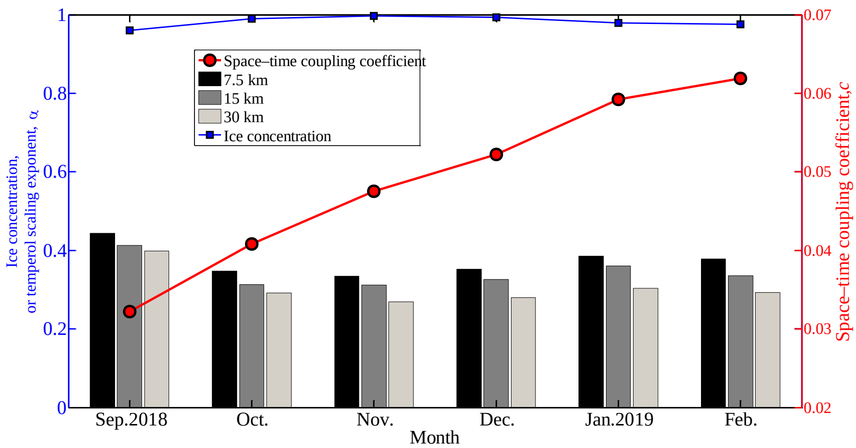

Figure 13 Changes in monthly temporal scaling exponent at various length scales, space–time coupling coefficient, and average ice concentration within the CHINARE buoy cluster.

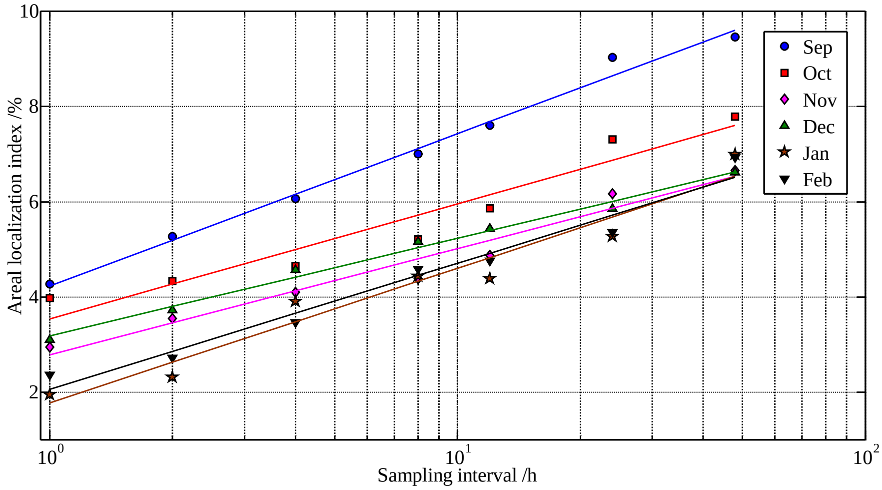

Figure 14 Changes in monthly (September 2018 to February 2019) areal localization index of ice deformation at a length scale of 10–20 km as a function of the position data resampling frequency.

https://doi.org/10.5194/tc-2020-211
Preprint. Discussion started: 25 August 2020

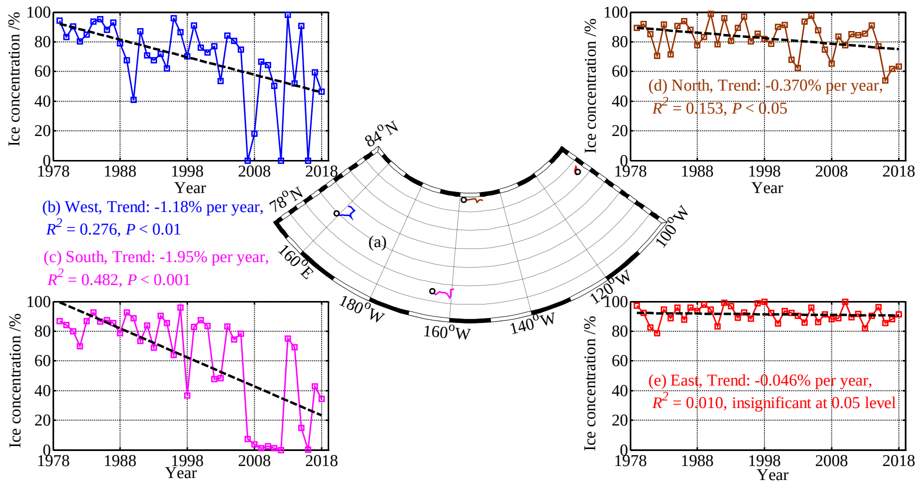

Figure 15 (a) Drift trajectories of the westernmost, southernmost, near northernmost, and easternmost buoys from 1 to 15 September 2018; the northernmost buoy has been omitted because it drifted to the north of 84.5° N, where SMMR ice concentration data prior to 1987 are unavailable; trajectory of the westernmost buoy was reconstructed using the NSIDC ice motion product because this buoy was deployed on 15 September 2018; (b–e) Long-term changes in ice concentration along buoy trajectories averaged over 1–15 September, with black lines denoting linear trends.

https://doi.org/10.5194/tc-2020-211
Preprint. Discussion started: 25 August 2020

770 Table 1. Statistical relationships between IWSR and selected parameters. Significance levels are $P <$
771 0.001 (***), $P < 0.01$ (**), and $P < 0.05$ (*), and n.s. denotes not significant at the 0.05 significance
772 level. Numbers in parentheses indicate number of buoys considered for the given period.

Month	vs. Lat.	vs. Lon.	vs. W_{10m}	vs. T_{2m}
20 Aug.-30 Sep.	–0.647**(24)	–0.738***(29)	–0.542**(32)	n.s.
Oct.	–0.811***(24)	–0.885***(29)	–0.866***(32)	0.657***(32)
Nov.	–0.777***(23)	–0.765***(28)	n.s.	0.736***(32)
Dec.	–0.736***(22)	–0.829***(27)	n.s.	0.675***(32)
Jan.	n.s.	–0.711**(23)	n.s.	n.s.
Feb.	n.s.	–0.610**(23)	n.s.	n.s.

773